aerospace

MDPI

Article

A Funnel-Based Framework for Quantitative Safety Metric Construction and Safety-Metric-Driven Control Synthesis of Automatic Carrier Landing Systems

Zhen Liu, Jianjun Luo, Yunzhao Liu and Weihua Ma *

National Key Laboratory of Aerospace Flight Dynamics, School of Astronautics, Northwestern Polytechnical University, Xi'an 710072, China
* Correspondence: whma_npu@nwpu.edu.cn

Abstract

Current research on Automatic Carrier Landing Systems (ACLSs) primarily focuses on guidance and control performance metrics. However, safety metrics that quantitatively characterize the safe region of ACLSs are equally crucial for guaranteeing safe landings, since safe and precise go-around decisions can only be made when the safe region is explicitly known. Therefore, this paper proposes a funnel-based framework that constructs quantitative safety metrics for making go-around decisions and quantitatively evaluating the safety of ACLSs. Additionally, safety-metric-driven control synthesis can be conducted to optimize controller parameters to maximize the safe region, i.e., to improve the safety of ACLSs. Specifically, the terminal landing requirements are formulated as a terminal set. Then, under the closed-loop dynamics with actuator saturation constraints and environmental disturbances, a funnel is constructed by sum-of-squares programming. Owing to its invariance property, all closed-loop trajectories starting inside the funnel converge to the terminal set, i.e., the terminal landing requirements are satisfied, and thus, the funnel serves as the safe region throughout the landing process. Furthermore, an online go-around decision rule is derived by checking whether the current state lies inside the offline-computed funnel. Simulation results validate the capability of the proposed framework to guarantee safe landings and further confirm its effectiveness under deck motion disturbance. Moreover, the funnel can serve as a larger safe region in the multi-dimensional state space than existing approaches based on a single state dimension, while constructing quantitative safety metrics for evaluating the safety of ACLSs. Finally, safety-metric-driven control synthesis demonstrates its ability to optimize controller parameters toward maximizing the safe region.

Keywords: carrier landing; go-around decision; safety metric; funnel; control synthesis; sum of squares programming

Check for updates

Academic Editor: Gokhan Inalhan

Received: 7 July 2026
Revised: 4 August 2026
Accepted: 7 August 2026
Published: 10 August 2026

Copyright: © 2026 by the authors. Licensee MDPI, Basel, Switzerland. This article is an open access article distributed under the terms and conditions of the Creative Commons Attribution (CC BY) license.

1. Introduction

Carrier landings are widely recognized as one of the most hazardous flight operations in carrier aviation. Compared with conventional land-based landings, significantly higher failure rates are involved, with landing-related mishaps constituting a major portion of overall carrier aviation mishaps [1]. Consequently, Automatic Carrier Landing Systems (ACLSs) have been developed as system-level implementations of guidance and control approaches to improve landing success rates.

Most studies on ACLSs have concentrated on enhancing the performance of the guidance and control system. However, for making go-around decisions, such improvement alone is not sufficient. The central issue is to explicitly characterize the safe region of ACLSs. In this paper, the safe region refers to a region in which the aircraft state can still be controlled by the closed-loop controller to satisfy the terminal landing requirements under actuator saturation constraints and environmental disturbances.

In practice, the boundary of the safe region is often represented by a single-dimensional altitude error tolerance along a nominal trajectory [2], which lacks the ability to characterize the multi-dimensional state constraints inherent in carrier landings. As a result, existing approaches cannot provide an explicit multi-dimensional safe region, let alone quantitatively evaluate it, leading to overly conservative or insufficiently precise go-around decisions.

In addition, quantitatively evaluating the safe region of ACLSs under stringent terminal landing precision requirements is further complicated by two intrinsic factors [1]. First, the closed-loop longitudinal dynamics of fixed-wing carrier aircraft are strongly nonlinear and highly coupled, with nonlinear aerodynamic effects that are considerably more complex than those of rotorcraft [3]. Second, the aircraft must operate in the presence of severe environmental disturbances, including atmospheric turbulence and deck motion, which introduce time-varying and stochastic effects that pose significant challenges to stability and robustness.

To cope with these challenges, a broad spectrum of control approaches has been investigated to enhance the closed-loop tracking performance in ACLSs. Early developments were dominated by classical linear techniques such as PID control [4] and robust control [5]. Although widely adopted in practice, their dependence on linearized models fundamentally restricts their ability to accommodate the strong nonlinearities of the dynamics. As a result, these limitations motivated the development of nonlinear control approaches, with dynamic inversion [6] and backstepping [7] serving as two foundational frameworks. Subsequently, a series of robustness-oriented control approaches, including adaptive control [8,9], adaptive sliding mode control [10], active disturbance rejection control [11], and neural network-based disturbance observers [12,13], have been proposed to better handle uncertainties. In parallel, prescribed performance control [14–17], fixed-time control [14–16], and control barrier function based control [17] have also been developed to restrict tracking errors. Furthermore, modern ACLS implementations commonly integrate several of these techniques into composite control architectures [5,8,12–21]. By contrast, another research direction pursues feedforward–feedback composite approaches [2], most notably preview control [22–24] and a wide range of model predictive control (MPC) formulations, such as output feedback stochastic MPC [25] and receding horizon control [26]. By optimizing control inputs online, these approaches provide improved adaptability in changing environments. However, their reliance on repeated real-time optimization introduces substantial computational demands, which hinder timely and reliable execution in highly dynamic scenarios such as carrier landing. Even in relatively mature applications like powered descent [27], the performance of rapid open-loop replanning remains fundamentally limited.

A recent comprehensive review identified the performance evaluation of Automatic Carrier Landing Systems and the design of safety-oriented go-around and escape decision methods as two key research problems in carrier landing, and further emphasized that the evaluation and safety assurance mechanisms of carrier landing systems require continued strengthening [2]. Consistent with these observations, existing ACLS research still lacks a unified framework that explicitly characterizes the multi-dimensional safe region, constructs quantitative safety metrics for evaluating different closed-loop control systems, and further employs these metrics to guide controller synthesis under complex nonlin-

ear dynamics and severe environmental disturbances. Accordingly, the main research hypothesis investigated in this study is that a funnel constructed for the closed-loop ACLS can serve as a unified quantitative representation of its time-varying multi-dimensional safe region, thereby supporting online go-around decisions, quantitative safety evaluation, and safety-metric-driven control synthesis. As a specific aspect of this hypothesis, under identical terminal landing requirements, actuator saturation constraints, and disturbance bounds, the multi-dimensional funnel is expected to provide a less conservative and more informative safety assessment than the conventional criterion based solely on altitude deviation. In this regard, the robust control invariant set (referred to as a tube for linear systems and a funnel for nonlinear systems) provides a theoretical foundation for constructing such safety metrics.

Originally introduced in robotic motion planning [28], the funnel captures all possible closed-loop trajectories around a nominal trajectory. Tedrake [29] first introduced sum-of-squares (SOS) programming to make funnel estimation tractable. Since then, funnel-based techniques have been extended to applications in spacecraft proximity operations [30] and planetary powered descent guidance [27]. As illustrated in Figure 1, the funnel represents a time-varying and multi-dimensional safe region around the nominal trajectory: all closed-loop trajectories starting inside the funnel at the current time instant successively evolve into the funnel at the following time instants and eventually converge to a terminal set that reflects the terminal landing requirements, while explicitly accounting for closed-loop nonlinear dynamics, actuator saturation constraints, and environmental disturbances. These properties make the funnel particularly well suited for carrier landings. When the current aircraft state remains inside the funnel, the aircraft continues the landing process; if it leaves the funnel, a go-around is initiated. Notably, such an exit event can only occur when actual disturbances exceed the bounds assumed during funnel estimation.

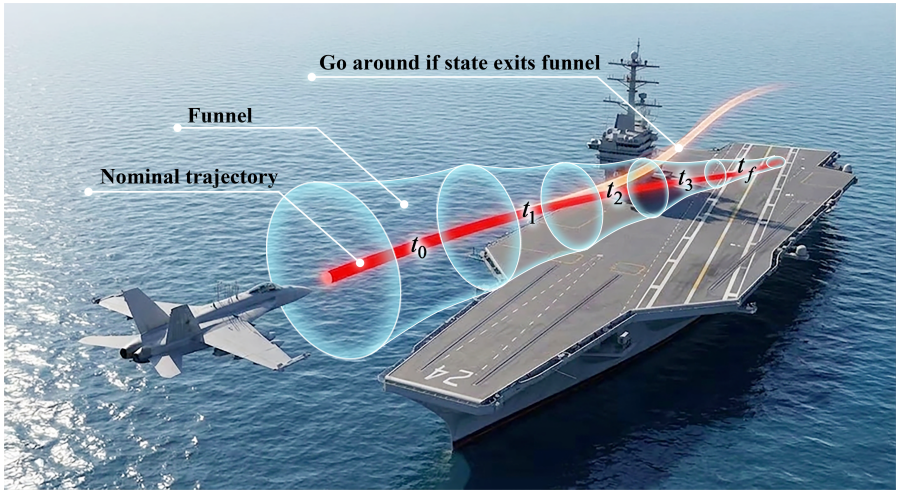


Figure 1. The funnel-based safety-guaranteed go-around framework. (Funnel represents the safe region).

Beyond funnel estimation, funnel control synthesis has also been explored, in which the controller and the funnel are jointly designed to enlarge the funnel volume. Liu et al. [31], for example, employed funnel control synthesis for powered descent, demonstrating that optimized closed-loop controllers can significantly expand the funnel and thereby improve robustness against initial state dispersions and disturbances.

Our earlier funnel-based studies on powered descent [27,31] focused on a different application scenario and therefore did not address the unique characteristics of ACLSs, such as complex nonlinear dynamics and severe environmental disturbances. More importantly,

the funnel was not exploited to derive go-around decision rules, nor was it integrated into a unified framework for quantitatively evaluating safety and synthesizing controllers.

Based on the above idea, the overall framework of this paper is shown in Figure 2. First, the terminal landing requirements are formulated as a terminal set, and the closed-loop ACLS dynamics are modeled with actuator saturation constraints and environmental disturbances. Then, a funnel is constructed offline by SOS programming to explicitly characterize the multi-dimensional safe region. Based on the obtained funnel, quantitative safety metrics are defined to evaluate the safety of ACLSs, and an online go-around decision rule is derived by checking whether the current aircraft state lies inside the offline-computed funnel. Finally, the safety metric is further incorporated into control synthesis, where controller parameters are optimized to enlarge the funnel and improve the safety of ACLSs by improving robustness against initial state dispersions and disturbances.

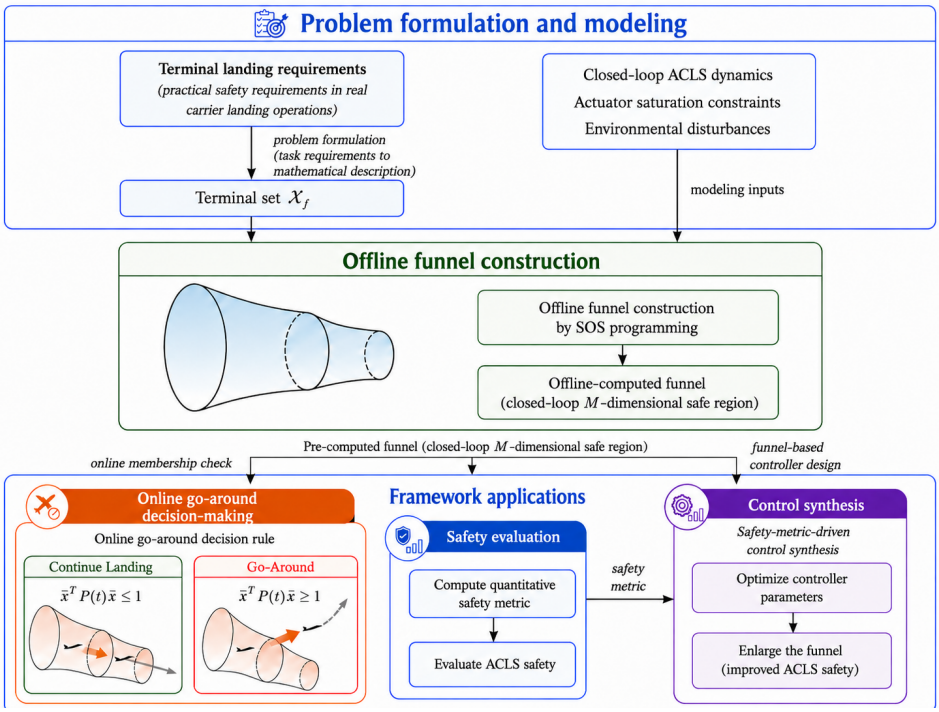


Figure 2. Overall framework of the proposed funnel-based go-around decision, safety metric construction, and safety-metric-driven control synthesis for ACLS.

In summary, to address the lack of quantitative safe region evaluation and safety-metric-driven controller synthesis in existing ACLSs research under complex nonlinear dynamics and severe environmental disturbances, this paper proposes a funnel-based safety-guaranteed go-around framework. The main contributions are as follows:

(1) A funnel-based go-around decision rule is developed. By explicitly characterizing the multi-dimensional safe region of ACLS through a funnel, the proposed method overcomes the limitation of traditional single-dimensional altitude deviation approaches and enables safer and more precise go-around decisions.
(2) A quantitative safety metric is established for ACLS. The funnel enables quantitative evaluation of safety for different closed-loop control systems through funnel volume and state-wise admissible deviations.
(3) Based on the proposed safety metric, a funnel-based controller synthesis approach is introduced to enlarge the safe region. By optimizing controller parameters with the funnel-based safety metric as the optimization criterion, larger funnel volume and improved state-wise admissible deviations can be achieved.

The remainder of the paper is structured as follows: Section 2 presents the dynamics model and the polynomial representation of the closed-loop system. Section 3 introduces the funnel definition and its safety interpretation. Section 4 develops the safety-guaranteed go-around decision framework, including the funnel-based safety metric and funnel-based control synthesis. Section 5 provides the simulation results and discussions. Finally, Section 6 concludes the paper.

2. Nonlinear Longitudinal Dynamics Model and Closed-Loop Polynomial Representation

This section introduces the nonlinear longitudinal dynamics model of the aircraft and the construction of a closed-loop polynomial system used for subsequent funnel-based analysis.

To describe the longitudinal motion of the aircraft during carrier landing, a nonlinear longitudinal dynamics model is adopted. The motion is described in the flight path coordinate system, where the longitudinal dynamics are given by [11]:

$$\begin{cases} \dot{V} = \dfrac{P_{\max} D_p \cos\alpha - C_D\, q\, S_{\text{ref}} - mg\sin\theta}{m} \\ \dot{\theta} = \dfrac{P_{\max} D_p \sin\alpha + C_L\, q\, S_{\text{ref}} - mg\cos\theta}{mV} \\ \dot{\vartheta} = \omega \\ \dot{\omega} = \dfrac{C_M\, q\, S_{\text{ref}}\, c}{I} \\ \dot{H} = V\sin\theta \\ \dot{L} = V\cos\theta \end{cases} \tag{1}$$

where $P_{\max}$ denotes the maximum thrust, and D_p denotes the throttle setting. The variables V, θ, ϑ, ω, H, and L represent the airspeed, flight path angle, pitch angle, pitch rate, altitude, and range, respectively. The angle of attack is denoted by α, and the dynamic pressure is denoted by q. The remaining parameters include the gravitational acceleration g, aircraft mass m, moment of inertia I, reference area S_{ref} and aerodynamic chord length c. The aerodynamic drag, lift, and pitching-moment coefficients, denoted by C_D, C_L, and C_M, respectively, are expressed as:

$$\begin{cases} C_D = C_{D0} + C_{D\alpha}\alpha + C_{D\alpha^2}\alpha^2 \\ C_L = C_{L0} + C_{L\alpha}\alpha + C_{LD_z} D_z \\ C_M = C_{M0} + C_{M\alpha}\alpha + C_{MD_z} D_z + C_{M\omega}\omega \end{cases} \tag{2}$$

where D_z denotes the elevator deflection.

Accordingly, the state vector and control vector for the dynamics model (1) are defined as:

$$\boldsymbol{x} = \begin{bmatrix} V & \theta & \vartheta & \omega & H & L \end{bmatrix}^\top, \qquad \boldsymbol{u} = \begin{bmatrix} D_z & D_p \end{bmatrix}^\top. \tag{3}$$

A nominal landing trajectory $\boldsymbol{x}_{\text{op}}(t)$ and the associated feedforward input $\boldsymbol{u}_{\text{op}}(t)$ are generated via trajectory optimization subject to the nonlinear dynamics in (1) and the actuator and terminal constraints, around which the closed-loop polynomial system is constructed. Specifically, the nominal trajectory is obtained offline by transcribing the following optimal control problem using GPOPS-II and solving it with SNOPT:

$$\begin{aligned}
&\text{find} \quad \boldsymbol{x}_{\text{op}}(t), \boldsymbol{u}_{\text{op}}(t) \\
&\min \quad J_{\text{op}} = \int_0^{t_f} \left(\frac{1}{2} D_z^2(t) + \frac{1}{2} D_p^2(t) \right) \mathrm{d}t \\
&\text{s.t.} \quad \dot{\boldsymbol{x}}_{\text{op}}(t) = \boldsymbol{f}\big(\boldsymbol{x}_{\text{op}}(t), \boldsymbol{u}_{\text{op}}(t)\big), \quad t \in [0, t_f] \\
&\quad \boldsymbol{x}_{\text{op}}(0) = \boldsymbol{x}_0 \\
&\quad \boldsymbol{x}_{\text{op}}(t_f) \in \mathcal{X}_{\text{op},f} \\
&\quad \boldsymbol{x}_{\min} \le \boldsymbol{x}_{\text{op}}(t) \le \boldsymbol{x}_{\max}, \quad t \in [0, t_f] \\
&\quad \boldsymbol{u}_{\min} \le \boldsymbol{u}_{\text{op}}(t) \le \boldsymbol{u}_{\max}, \quad t \in [0, t_f].
\end{aligned} \tag{4}$$

Here, $\boldsymbol{f}$ denotes the right-hand side of the nonlinear dynamics in (1), $\boldsymbol{x}_0$ denotes the prescribed initial state, and $\mathcal{X}_{\text{op},f}$ denotes the admissible terminal-state set specified by the terminal landing requirements for nominal trajectory generation.

Based on the nominal trajectory, the closed-loop system is represented in terms of state deviations. Specifically, the actual state and control input are decomposed into nominal components and deviation terms as:

$$\boldsymbol{x}(t) = \boldsymbol{x}_{\text{op}}(t) + \bar{\boldsymbol{x}}(t) \tag{5}$$

$$\boldsymbol{u}(t) = \boldsymbol{u}_{\text{op}}(t) + \bar{\boldsymbol{u}}(t) \tag{6}$$

where $\bar{\boldsymbol{x}}(t)$ and $\bar{\boldsymbol{u}}(t)$ denote the state and control deviations from the nominal trajectory.

In the neighborhood of the nominal trajectory, a linear state feedback law is considered:

$$\bar{\boldsymbol{u}}(t) = -\boldsymbol{K}(t)\bar{\boldsymbol{x}}(t) \tag{7}$$

where $\boldsymbol{K}(t)$ is the time-varying feedback gain matrix. Substituting the closed-loop control input into the nonlinear dynamics, the closed-loop dynamics can be written as:

$$\boldsymbol{g}(\bar{\boldsymbol{x}}, t) = \boldsymbol{f}\big(\boldsymbol{x}_{\text{op}}(t) + \bar{\boldsymbol{x}}(t), \boldsymbol{u}_{\text{op}}(t) - \boldsymbol{K}(t)\bar{\boldsymbol{x}}(t)\big). \tag{8}$$

Then, the error dynamics are obtained by subtracting the nominal dynamics:

$$\dot{\bar{\boldsymbol{x}}} = \boldsymbol{g}(\bar{\boldsymbol{x}}, t) - \boldsymbol{f}\big(\boldsymbol{x}_{\text{op}}(t), \boldsymbol{u}_{\text{op}}(t)\big) \triangleq \boldsymbol{F}(\bar{\boldsymbol{x}}, t). \tag{9}$$

To use the SOS programming method for funnel construction, the error dynamics need to be approximated as polynomial functions. In this work, a second-order Taylor expansion is performed around the nominal trajectory $\bar{\boldsymbol{x}} = \boldsymbol{0}$. For the i-th state component, the polynomial approximation is written as:

$$p_i(\bar{\boldsymbol{x}}, t) = F_i(\boldsymbol{0}, t) + \boldsymbol{J}_i^{\mathrm{T}}(t)\bar{\boldsymbol{x}} + \frac{1}{2}\bar{\boldsymbol{x}}^{\mathrm{T}}\boldsymbol{H}_i(t)\bar{\boldsymbol{x}}, \qquad i = 1, \ldots, 6 \tag{10}$$

where:

$$\boldsymbol{J}_i(t) = \left.\frac{\partial F_i}{\partial \bar{\boldsymbol{x}}}\right|_{\bar{\boldsymbol{x}}=\boldsymbol{0}}, \qquad \boldsymbol{H}_i(t) = \left.\frac{\partial^2 F_i}{\partial \bar{\boldsymbol{x}} \partial \bar{\boldsymbol{x}}^{\mathrm{T}}}\right|_{\bar{\boldsymbol{x}}=\boldsymbol{0}}. \tag{11}$$

Collecting all state components, the closed-loop polynomial system used for subsequent funnel construction is obtained as:

$$\dot{\bar{\boldsymbol{x}}} \approx \boldsymbol{p}(\bar{\boldsymbol{x}}, t). \tag{12}$$

3. Funnel Definition and Safety Interpretation

A funnel is a time-varying finite-time invariant set defined along a nominal trajectory that characterizes the evolution of the closed-loop system. In the present paper, the backward funnel is constructed for the closed-loop polynomial system introduced in Section 2. Intuitively, it describes a region in the state deviation space such that, if the current state lies inside this region at a given time, the subsequent closed-loop trajectory is guaranteed to evolve toward a prescribed terminal set under the considered actuator saturation constraints, terminal landing requirements, and disturbance bounds. Therefore, the funnel can be interpreted as a time-varying multi-dimensional safe region for go-around decisions, and it also provides the basis for subsequent safety evaluation and control synthesis.

3.1. Funnel Representation and Finite-Time Invariance

To provide a concrete mathematical representation, the funnel at time $t \in [0, t_f]$ is described as an n-dimensional ellipsoidal set along the nominal trajectory, where n denotes the state dimension:

$$F(t) = \left\{ \bar{\boldsymbol{x}} \mid V(\bar{\boldsymbol{x}}, t) \triangleq \bar{\boldsymbol{x}}^\top \boldsymbol{P}(t) \bar{\boldsymbol{x}} \leq 1 \right\}. \tag{13}$$

where $\boldsymbol{P}(t)$ is a symmetric positive-definite matrix characterizing the size and shape of the funnel, and $V(\bar{\boldsymbol{x}}, t)$ is the corresponding level-set function.

In numerical implementation, the continuous-time funnel is represented by a finite sequence of ellipsoidal sets at discrete time instants $t_k \in [0, t_f], k = 1, \ldots, N$:

$$F(t_k) = \left\{ \bar{\boldsymbol{x}} \mid V_k(\bar{\boldsymbol{x}}) \triangleq \bar{\boldsymbol{x}}^\top \boldsymbol{P}_k \bar{\boldsymbol{x}} \leq 1 \right\}, \qquad k = 1, \ldots, N. \tag{14}$$

Each matrix $\boldsymbol{P}_k$ specifies the ellipsoidal set at time t_k. Therefore, the backward funnel construction can be regarded as the sequential computation of these shape matrices from the terminal time to the initial time. In the following SOS construction and numerical implementation, the discrete-time notation $F(t_k)$ and $V_k(\bar{\boldsymbol{x}})$ is used unless otherwise stated.

When bounded environmental disturbances, modeling errors, or Taylor truncation errors are considered, the closed-loop polynomial system in (12) can be written as:

$$\dot{\bar{\boldsymbol{x}}} = \boldsymbol{p}(\bar{\boldsymbol{x}}, t, \boldsymbol{w}), \qquad \boldsymbol{w} \in W, \tag{15}$$

where $\boldsymbol{w}$ denotes the bounded term introduced for the considered effect, and W denotes the corresponding prescribed bounded set. In the proposed method, different bounded effects can be handled in this form by specifying the corresponding $\boldsymbol{w}$ and W. In particular, the invariance guarantee is established for the closed-loop polynomial approximation. If the Taylor truncation error is bounded and included in W, the same SOS condition provides a conservative invariance guarantee under the corresponding bounded approximation error.

The key property underlying the safety interpretation of the funnel is finite-time invariance. In continuous time, this means that, if the state deviation starts from the funnel at any time $\tau \in [0, t_f]$, then the subsequent closed-loop trajectory remains inside the corresponding funnel over the remaining time horizon:

$$\bar{\boldsymbol{x}}(\tau) \in F(\tau) \quad \Rightarrow \quad \bar{\boldsymbol{x}}(t) \in F(t), \qquad \forall\, t \in [\tau, t_f]. \tag{16}$$

In the discrete implementation, this property is enforced on the time grid $t_k{}_{k=1}^{N}$. If $\bar{\boldsymbol{x}}(t_k) \in F(t_k)$, finite-time invariance guarantees that the subsequent trajectory satisfies $\bar{\boldsymbol{x}}(t_j) \in F(t_j)$ for $j = k+1, \ldots, N$ and finally reaches the terminal set $\mathcal{X}_f$. Therefore, finite-time invariance links membership in the funnel at the current time instant to the satisfaction of the terminal landing requirements.

For the normalized funnel in (13), finite-time invariance can be guaranteed by imposing the following boundary condition:

$$V(\bar{\boldsymbol{x}}, t) = 1 \quad \Rightarrow \quad \dot{V}(\bar{\boldsymbol{x}}, t, \boldsymbol{w}) \leq 0, \qquad \forall\, \boldsymbol{w} \in W. \tag{17}$$

where the total derivative of the time-varying level-set function along the closed-loop trajectory is given by:

$$\dot{V}(\bar{\boldsymbol{x}}, t, \boldsymbol{w}) = \nabla_{\bar{x}} V(\bar{\boldsymbol{x}}, t)^{\top} \boldsymbol{p}(\bar{\boldsymbol{x}}, t, \boldsymbol{w}) + \frac{\partial V(\bar{\boldsymbol{x}}, t)}{\partial t}. \tag{18}$$

This condition means that the value of $V(\bar{\boldsymbol{x}}, t)$ does not increase when the trajectory reaches the funnel boundary. Therefore, the trajectory cannot cross the boundary outward, and the funnel remains invariant over the finite time horizon for all bounded effects included in W.

3.2. Terminal Set and Backward Funnel Construction

The terminal set is defined as:

$$\mathcal{X}_f = \left\{ \bar{\boldsymbol{x}} \,\middle|\, \bar{\boldsymbol{x}}^{\top} \boldsymbol{E} \bar{\boldsymbol{x}} \leq 1 \right\}, \tag{19}$$

where $\boldsymbol{E}$ is a symmetric positive-definite matrix that determines the shape of the terminal set. By appropriately selecting $\boldsymbol{E}$, different terminal landing requirements can be imposed on individual state components at the final time. If the terminal funnel satisfies:

$$F(t_f) \subseteq \mathcal{X}_f, \tag{20}$$

then every trajectory starting inside the funnel is guaranteed to reach the terminal set at t_f. Therefore, the funnel guarantees not only safety during the landing process, but also satisfaction of the prescribed terminal landing requirements.

In addition to the terminal landing requirements, actuator saturation constraints and bounded effects can also be incorporated into the SOS-based funnel construction. The saturation constraints are imposed to ensure that the feedback control input remains within the prescribed actuator bounds for all state deviations inside the funnel. The bounded term $\boldsymbol{w}$ is handled by requiring the invariance condition to hold for all admissible values in W. Therefore, the computed funnel should not be interpreted merely as a geometric envelope around the nominal trajectory. Instead, it represents a certified time-varying safe region of the closed-loop system under the considered terminal landing requirements, actuator saturation constraints, and bounded effects included in W.

To make the SOS formulation explicit, suppose that the bounded set W can be described by polynomial inequalities:

$$W = \left\{ \boldsymbol{w} \mid g_j(\boldsymbol{w}) \geq 0,\ j = 1, \ldots, n_w \right\}. \tag{21}$$

At each discrete time instant, the total derivative of the level-set function is evaluated as:

$$\begin{aligned} \dot{V}_k(\bar{\boldsymbol{x}}, \boldsymbol{w}) &= 2\bar{\boldsymbol{x}}^{\top} \boldsymbol{P}_k \boldsymbol{p}(\bar{\boldsymbol{x}}, t_k, \boldsymbol{w}) + \bar{\boldsymbol{x}}^{\top} \dot{\boldsymbol{P}}_k \bar{\boldsymbol{x}}, \\ \dot{\boldsymbol{P}}_k &\approx \frac{\boldsymbol{P}_{k+1} - \boldsymbol{P}_k}{t_{k+1} - t_k}. \end{aligned} \tag{22}$$

The second relation approximates the time variation of the funnel using adjacent time instants and therefore couples the funnel at t_k with the already computed funnel at t_{k+1}.

At the discrete time instant t_k, the boundary condition:

$$V_k(\bar{\boldsymbol{x}}) = 1, \quad \boldsymbol{w} \in W \quad \Rightarrow \quad \dot{V}_k(\bar{\boldsymbol{x}}, \boldsymbol{w}) \leq 0 \tag{23}$$

can be represented by the following SOS condition:

$$-\dot{V}_k(\bar{\boldsymbol{x}}, \boldsymbol{w}) - L_{Ik}(\bar{\boldsymbol{x}}, \boldsymbol{w})(1 - V_k(\bar{\boldsymbol{x}})) - \sum_{j=1}^{n_w} L_{Wjk}(\bar{\boldsymbol{x}}, \boldsymbol{w}) g_j(\boldsymbol{w}) \quad \text{is SOS,} \tag{24}$$

where $L_{Ik}(\bar{\boldsymbol{x}}, \boldsymbol{w})$ is a polynomial multiplier associated with the funnel boundary condition, and $L_{Wjk}(\bar{\boldsymbol{x}}, \boldsymbol{w})$, $j = 1, \ldots, n_w$, are SOS multiplier polynomials associated with the bounded set W. This condition provides a representative SOS inequality used to enforce the funnel invariance condition under the prescribed bounded set W.

The actuator saturation constraints can be imposed in a similar SOS form. For example, if the i-th control input at time t_k is denoted by $u_{i,k}(\bar{\boldsymbol{x}})$ and satisfies the prescribed limits $u_{i,\min} \leq u_{i,k} \leq u_{i,\max}$, then the implication:

$$\bar{\boldsymbol{x}} \in F(t_k) \quad \Rightarrow \quad u_{i,\min} \leq u_{i,k}(\bar{\boldsymbol{x}}) \leq u_{i,\max} \tag{25}$$

can be enforced by requiring:

$$\begin{aligned} u_{i,k}(\bar{\boldsymbol{x}}) - u_{i,\min} - L_{ik}^{L}(\bar{\boldsymbol{x}})(1 - V_k(\bar{\boldsymbol{x}})) \quad &\text{is SOS,} \\ u_{i,\max} - u_{i,k}(\bar{\boldsymbol{x}}) - L_{ik}^{U}(\bar{\boldsymbol{x}})(1 - V_k(\bar{\boldsymbol{x}})) \quad &\text{is SOS,} \end{aligned} \tag{26}$$

where $L_{ik}^{L}(\bar{\boldsymbol{x}})$ and $L_{ik}^{U}(\bar{\boldsymbol{x}})$ are SOS multiplier polynomials. Here, $u_{i,k}(\bar{\boldsymbol{x}})$ denotes the total control input, including the nominal input and the deviation feedback input. These constraints ensure that the total control input generated by the specified feedback law remains within the prescribed actuator bounds for all state deviations inside the funnel. Therefore, states for which the specified feedback law would produce an input outside the actuator bounds are excluded from the computed funnel, although such states might still reach the terminal set under another admissible control law.

Following the point-by-point backward construction strategy, the funnel at time t_k is computed based on the already obtained funnel at the next time instant t_{k+1}. Since the purpose of funnel estimation is to provide a meaningful quantitative characterization of the certified safe region associated with the given closed-loop controller, merely finding an arbitrary feasible funnel is insufficient. Therefore, after an initial feasible funnel is obtained, it is further enlarged through an alternating optimization procedure following the strategy in [27].

For the normalized representation in (14), the size of the ellipsoidal funnel is proportional to $\det(\boldsymbol{P}_k)^{-1/2}$. Directly maximizing this quantity is difficult within the SOS optimization framework. Therefore, a fixed positive-definite matrix $\boldsymbol{S}_k$ and a positive relaxation coefficient σ_k are introduced such that:

$$\boldsymbol{P}_k \preceq \sigma_k \boldsymbol{S}_k. \tag{27}$$

Accordingly, the auxiliary ellipsoid:

$$\left\{ \bar{\boldsymbol{x}} \mid \bar{\boldsymbol{x}}^{\top} \sigma_k \boldsymbol{S}_k \bar{\boldsymbol{x}} \leq 1 \right\} \tag{28}$$

is contained in $F(t_k)$. Minimizing σ_k enlarges this inner ellipsoid and thereby provides a heuristic means of enlarging the funnel. In the numerical implementation, $\boldsymbol{S}_k$ is taken as the identity matrix.

Given $F(t_{k+1})$ and $\boldsymbol{S}_k$, the local funnel-estimation problem at time t_k is summarized as:

$$\begin{aligned} \text{given} \quad & F(t_{k+1}),\ \boldsymbol{S}_k, \\ \text{find} \quad & \boldsymbol{P}_k,\ \mathcal{L}_k,\ \sigma_k, \\ \text{minimize} \quad & \sigma_k, \\ \text{s.t.} \quad & \boldsymbol{P}_k \succ 0, \quad \sigma_k > 0, \\ & \boldsymbol{P}_k \preceq \sigma_k \boldsymbol{S}_k, \\ & \text{the funnel invariance SOS constraint,} \\ & \text{the actuator saturation SOS constraints,} \\ & \text{the bounded effect SOS constraints.} \end{aligned} \tag{29}$$

Here, $\mathcal{L}_k$ denotes the collection of multiplier polynomials at time t_k.

The terminal condition for the backward recursion is specified by (19) and (20). Specifically, the backward construction starts from:

$$F(t_N) = \mathcal{X}_f, \qquad \boldsymbol{P}_N = \boldsymbol{E}, \qquad t_N = t_f, \tag{30}$$

and then proceeds backward to compute $F(t_{N-1}), F(t_{N-2}), \ldots, F(t_1)$.

Problem (29) is not solved simultaneously for $\boldsymbol{P}_k$ and $\mathcal{L}_k$, because the funnel invariance condition contains bilinear products between the shape matrix and the SOS multipliers. Instead, a bilinear alternating search is adopted. At each time instant, the shape matrix is first initialized using the already computed matrix at the next time instant. With the shape matrix fixed, the multiplier polynomials are solved to establish feasibility. If no feasible multipliers can be found, the current ellipsoid is reduced by multiplying $\boldsymbol{P}_k$ by a roll-back factor $b > 1$, and the feasibility search is repeated. Once a feasible solution is obtained, the multipliers are fixed and $\boldsymbol{P}_k$ is optimized by minimizing σ_k. The multipliers and the shape matrix are then alternately updated until the improvement in the funnel size falls below a prescribed threshold. The corresponding computation procedure is summarized in Table 1.

Table 1. Point-by-point backward funnel estimation procedure.

Step	Procedure
Step 0	Specify the terminal condition and solution parameters. Choose the discrete time grid $\{t_k\}_{k=1}^{N}$, set $t_N = t_f$ and $\boldsymbol{P}_N = \boldsymbol{E}$, and specify the convergence threshold $\varepsilon > 0$ and roll-back factor $b > 1$.
Step 1	Initialize the shape matrix. For $k = N-1, N-2, \ldots, 1$, initialize the current shape matrix as $\boldsymbol{P}_k = \boldsymbol{P}_{k+1}$.
Step 2	Obtain a feasible shape matrix. With $\boldsymbol{P}_{k+1}$ and $\boldsymbol{P}_k$ fixed, solve the SOS multiplier subproblem to obtain $\mathcal{L}_k$. If the SOS constraints are infeasible, set $\boldsymbol{P}_k = b\boldsymbol{P}_k$ and repeat this step.
Step 3	Optimize the shape matrix. With $\mathcal{L}_k$ fixed, minimize σ_k subject to the SOS constraints and $\boldsymbol{P}_k \preceq \sigma_k \boldsymbol{S}_k$ to obtain an updated $\boldsymbol{P}_k$.
Step 4	Check convergence. Evaluate the funnel-size indicator $\det(\boldsymbol{P}_k)^{-1/2}$. If its relative improvement is smaller than ε, proceed to t_{k-1}; otherwise, continue to Step 5.
Step 5	Update the SOS multipliers. With the updated $\boldsymbol{P}_k$ fixed, solve the SOS multiplier subproblem to update $\mathcal{L}_k$, and then return to Step 3.

4. Funnel-Based Safety-Guaranteed Go-Around Framework

The proposed funnel-based safety-guaranteed go-around framework consists of an offline computation stage and an online implementation stage.

4.1. Funnel-Based Go-Around Decision Rule

In the offline stage, a nominal landing trajectory is generated as described in Section 2, around which a backward funnel is constructed according to Section 3. The obtained funnel characterizes a time-varying safe region while explicitly accounting for nonlinear dynamics, actuator saturation constraints, terminal landing requirements, and disturbance bounds. Based on the constructed funnel, quantitative safety evaluation can be carried out for a given closed-loop control system, and safety-metric-driven control synthesis can further be performed to enlarge the safe region, thereby improving robustness against initial state dispersions and disturbances.

During the online stage, the carrier aircraft acquires its current state at each sampling instant t_k and computes the state deviation $\bar{\boldsymbol{x}}(t_k) = \boldsymbol{x}(t_k) - \boldsymbol{x}_{\mathrm{op}}(t_k)$. The online go-around decision is then made by checking whether the current aircraft state lies inside the offline-computed funnel around the nominal trajectory. Specifically, the decision rule is written as:

$$V_k(\bar{\boldsymbol{x}}(t_k)) = \bar{\boldsymbol{x}}^\top(t_k)\boldsymbol{P}_k\bar{\boldsymbol{x}}(t_k) \leq 1 \Rightarrow \text{continue landing}, \tag{31}$$

$$V_k(\bar{\boldsymbol{x}}(t_k)) = \bar{\boldsymbol{x}}^\top(t_k)\boldsymbol{P}_k\bar{\boldsymbol{x}}(t_k) > 1 \Rightarrow \text{go around}. \tag{32}$$

According to the invariance property established in Section 3, if $V_k(\bar{\boldsymbol{x}}(t_k)) \leq 1$ holds, the current aircraft state belongs to the offline-computed funnel at time t_k. Under the disturbance bounds and constraints considered in the offline funnel construction, the subsequent closed-loop trajectory is then guaranteed to remain inside the time-varying funnel and reach the terminal set at the final time. Therefore, the above scalar inequality provides an explicit and implementable link between the online go-around decision and the offline safety guarantee.

Beyond its role in online go-around decision making, the funnel also supports safety evaluation and control synthesis at the system design level. As described in Section 3, the computed funnel is represented by a sequence of ellipsoidal sets at discrete time instants along the nominal trajectory. Each ellipsoidal set characterizes the safe region at the corresponding time instant in the multi-dimensional state space. Therefore, its geometric properties, including the overall funnel volume and the admissible bounds along individual state dimensions, can be used to define quantitative safety metrics for evaluating a given closed-loop control system. In this sense, funnel-based analysis enables offline comparison of different control system designs and further supports safety-metric-driven control synthesis.

It should be emphasized that the funnel boundary should not be interpreted as the actual tracking-error boundary of the aircraft. Instead, it represents the boundary of the safe region characterized by the closed-loop controller under the prescribed terminal landing requirements, actuator saturation constraints, and disturbance bounds. The terminal landing requirements, actuator saturation constraints, and disturbance bounds are prescribed independently of the controller and serve as the safety-related criteria of the landing task. By contrast, whether a given aircraft state can still be driven to the terminal set while satisfying these prescribed requirements and constraints depends on the closed-loop dynamics and therefore on the implemented controller. For this reason, the safe region characterized by the funnel is controller-dependent. Under the same conditions, a larger funnel means that the closed-loop system has a larger safe region in the multi-dimensional state space while still guaranteeing convergence to the terminal set. Therefore, a larger funnel indicates a

larger safety margin, rather than poorer tracking performance. The actual tracking behavior is reflected by the closed-loop trajectories in the simulations, whereas the funnel volume quantifies the size of the safe region.

4.2. Funnel-Based Safety Metric

In this subsection, funnel-based safety metrics are established for evaluating the safety of the closed-loop system during the landing process. As described in Section 3, the continuous-time funnel is represented by a finite sequence of ellipsoidal sets $F(t_k)$ at discrete time instants along the nominal trajectory. These ellipsoidal sets characterize the safe region at the corresponding time instants in the multi-dimensional state space. For the dynamics model considered in this paper, the state dimension is $n = 6$, with $\boldsymbol{x} = [V, \theta, \vartheta, \omega, H, L]^\top$. The low-dimensional plots used in the simulations are only projections for visualization, whereas the safety metrics defined in this subsection are computed from the full-dimensional ellipsoidal sets.

Based on the ellipsoidal set $F(t_k)$ defined in Section 3, the funnel volume metric can be derived from the standard volume formula of an n-dimensional ellipsoid. Here, the term volume is used in the standard mathematical sense for an n-dimensional set. It corresponds to an area when $n = 2$ and to the usual three-dimensional volume when $n = 3$. In this paper, since the state dimension is $n = 6$, the funnel volume measures the size of the safe region in the six-dimensional state space, rather than the three-dimensional physical volume of the aircraft position space or the area or volume of any low-dimensional projection used for visualization.

For an ellipsoid of the following form:

$$\bar{\boldsymbol{x}}^\top \boldsymbol{P}_k \bar{\boldsymbol{x}} \leq 1, \tag{33}$$

where $\boldsymbol{P}_k$ is symmetric positive-definite, and its n-dimensional volume is given by:

$$\mathrm{Vol}(F(t_k)) = \frac{c_n}{\sqrt{\det(\boldsymbol{P}_k)}}, \qquad c_n = \frac{\pi^{n/2}}{\Gamma(n/2+1)}, \tag{34}$$

where c_n is the volume of the unit ball in the n-dimensional Euclidean space. Taking the logarithm gives:

$$\log \mathrm{Vol}(F(t_k)) = \log c_n - \frac{1}{2} \log \det(\boldsymbol{P}_k). \tag{35}$$

Since c_n is a constant for a fixed state dimension, the determinant-based quantity $-\log\det(\boldsymbol{P}_k)$ is monotonically related to the ellipsoidal volume. Accordingly, the funnel volume metric is defined as:

$$J_{\mathrm{vol}}(t_k) = -\log \det(\boldsymbol{P}_k). \tag{36}$$

A larger value of $J_{\mathrm{vol}}(t_k)$ indicates a larger safe region in the multi-dimensional state space under the same terminal landing requirements, actuator saturation constraints, and disturbance bounds.Since the state components have different physical units, the funnel volume metric is used as a relative comparison measure under the same state definition, units, and scaling, rather than as an absolute physical volume.

When control synthesis is considered, the funnel at time t_k is characterized jointly by $\boldsymbol{P}_k$ and ρ_k as:

$$F_{\mathrm{syn}}(t_k) = \left\{ \bar{\boldsymbol{x}} \mid \bar{\boldsymbol{x}}^\top \boldsymbol{P}_k \bar{\boldsymbol{x}} \leq \rho_k \right\} = \left\{ \bar{\boldsymbol{x}} \mid \bar{\boldsymbol{x}}^\top \left(\frac{\boldsymbol{P}_k}{\rho_k} \right) \bar{\boldsymbol{x}} \leq 1 \right\}. \tag{37}$$

Accordingly, the corresponding funnel volume metric is defined as:

$$J_{\mathrm{vol}}^{\mathrm{syn}}(t_k) = -\log\det\left(\frac{\boldsymbol{P}_k}{\rho_k}\right). \tag{38}$$

This metric provides a consistent basis for comparing the corresponding funnel volumes of different controllers under identical terminal landing requirements, actuator saturation constraints, and disturbance bounds. Therefore, if one controller yields a larger value of $J_{\mathrm{vol}}^{\mathrm{syn}}(t_k)$ than another controller, it means that the corresponding closed-loop system has a larger safe region at time t_k under the same conditions.

To illustrate how the funnel volume is calculated from the variables obtained by the control synthesis procedure, consider a discrete time instant t_k. Once $\boldsymbol{P}_k$ and ρ_k are obtained, the funnel is equivalently represented by the matrix $\boldsymbol{P}_k/\rho_k$. For the six-dimensional system considered in this paper, the corresponding funnel volume is calculated as:

$$\mathrm{Vol}\big(F_{\mathrm{syn}}(t_k)\big) = \frac{\pi^3}{6\sqrt{\det(\boldsymbol{P}_k/\rho_k)}}. \tag{39}$$

The corresponding funnel volume metric is then obtained from the same determinant according to the preceding definition. Thus, both the funnel volume and the corresponding metric are directly calculated from the funnel variables obtained at each time instant of the control synthesis procedure.

In addition to this global metric, state-wise metrics are introduced to quantify the admissible deviation bounds along individual state dimensions. Let $\boldsymbol{e}_i$ denote the i-th standard basis vector. For the ellipsoidal set determined by $\boldsymbol{P}_k$, the maximum admissible absolute value of the i-th state component is obtained by projecting the ellipsoidal set onto the i-th coordinate axis. Specifically, this bound is obtained from:

$$\max_{\bar{\boldsymbol{x}}} \quad \left|\boldsymbol{e}_i^{\top}\bar{\boldsymbol{x}}\right| \qquad \text{s.t.} \quad \bar{\boldsymbol{x}}^{\top}\boldsymbol{P}_k\bar{\boldsymbol{x}} \le 1. \tag{40}$$

By applying the Cauchy–Schwarz inequality, the optimal value is:

$$J_i(t_k) = \sqrt{\boldsymbol{e}_i^{\top}\boldsymbol{P}_k^{-1}\boldsymbol{e}_i} = \sqrt{\left(\boldsymbol{P}_k^{-1}\right)_{ii}}, \qquad i = 1,\ldots,n. \tag{41}$$

Here, $\left(\boldsymbol{P}_k^{-1}\right)_{ii}$ denotes the (i,i)-th diagonal element of $\boldsymbol{P}_k^{-1}$.It should be noted that $J_i(t_k)$ is the half-width of the projection of the full-dimensional ellipsoid onto the i-th coordinate axis. It does not represent an independent single-dimensional tolerance obtained by setting all other state deviations to zero.

For the control synthesis case, the ellipsoidal set is equivalently determined by $\boldsymbol{P}_k/\rho_k$. Therefore, the corresponding state-wise metric is defined as:

$$J_i^{\mathrm{syn}}(t_k) = \sqrt{\left[\left(\frac{\boldsymbol{P}_k}{\rho_k}\right)^{-1}\right]_{ii}}, \qquad i = 1,\ldots,n. \tag{42}$$

These quantities represent the admissible deviation bounds along individual state dimensions derived from the full-dimensional ellipsoidal safe region. They provide physically interpretable state-wise safety metrics, while still being obtained from the multi-dimensional safe region rather than from an isolated single-dimensional criterion.

Therefore, the funnel-based safety metrics evaluate the closed-loop system from two complementary aspects. The funnel volume metric reflects the overall size of the safe region in the multi-dimensional state space, while the state-wise metrics quantify the admissible

deviation bounds along individual state dimensions. Because these two types of metrics characterize different geometric properties of the same six-dimensional ellipsoidal safe region, their relative improvements are not directly comparable in magnitude. Together, these metrics provide a quantitative basis for evaluating and comparing the safety of different closed-loop control systems.

4.3. Funnel-Based Control Synthesis

Beyond safety evaluation, the funnel also provides a systematic framework for control synthesis. In this framework, the feedback gains are optimized together with the funnel variables to enlarge the certified safe region of the closed-loop system while satisfying the closed-loop dynamics, actuator saturation constraints, disturbance bounds, and terminal landing requirements. In this sense, the proposed synthesis method extends the framework from safety evaluation to safety-metric-driven control synthesis.

For a given nominal landing trajectory, the structure of the feedback control law is fixed, while the feedback gains are treated as decision variables in the funnel construction process. Specifically, the deviation control input at the discrete time instant t_k is written as:

$$\bar{\boldsymbol{u}}(t_k) = -\boldsymbol{K}_k \bar{\boldsymbol{x}}(t_k), \tag{43}$$

where $\bar{\boldsymbol{x}}(t_k) \in \mathbb{R}^6$ and $\bar{\boldsymbol{u}}(t_k) \in \mathbb{R}^2$. Accordingly, the time-varying feedback gain matrix satisfies $\boldsymbol{K}_k \in \mathbb{R}^{2\times 6}$ and can be written as:

$$\boldsymbol{K}_k = \begin{bmatrix} k_{11}(t_k) & k_{12}(t_k) & k_{13}(t_k) & k_{14}(t_k) & k_{15}(t_k) & k_{16}(t_k) \\ k_{21}(t_k) & k_{22}(t_k) & k_{23}(t_k) & k_{24}(t_k) & k_{25}(t_k) & k_{26}(t_k) \end{bmatrix}. \tag{44}$$

For the control synthesis considered in this paper, the 12 entries of $\boldsymbol{K}_k$ are directly optimized at each nonterminal discrete time instant t_k, $k = 1, \ldots, N-1$, while the terminal feedback gain is kept fixed. Thus, the synthesis procedure directly optimizes the time-varying feedback gains rather than retuning the LQR weighting matrices. At each nonterminal time instant, the feedback control law is substituted into the polynomial error dynamics described in Section 2. Consequently, $\boldsymbol{K}_k$ enters the SOS constraints through both the resulting closed-loop dynamics and the feedback control input: the former determines the funnel invariance condition, while the latter determines the actuator saturation constraints. Different values of $\boldsymbol{K}_k$ therefore lead to different closed-loop dynamics and different feasible funnels.

To provide an additional degree of freedom during control synthesis, the funnel at t_k is equivalently parameterized as:

$$F_{\text{syn}}(t_k) = \left\{ \bar{\boldsymbol{x}} \,\middle|\, \bar{\boldsymbol{x}}^\top \boldsymbol{P}_k \bar{\boldsymbol{x}} \le \rho_k \right\}, \tag{45}$$

where $\boldsymbol{P}_k \succ 0$ and $\rho_k > 0$. This representation is equivalent to the normalized funnel representation introduced in Section 3, since the level-set boundary ρ_k can be absorbed into the shape matrix through $\boldsymbol{P}_k/\rho_k$. The introduction of ρ_k therefore does not change the definition of the funnel, but provides an additional optimization variable for the synthesis procedure.

In the present paper, the funnel volume metric defined in Section 4.2 is adopted as the optimization criterion for control synthesis. Accordingly, the synthesis problem over the discrete time grid can be compactly formulated as:

$$
\begin{aligned}
\max_{\{\boldsymbol{K}_k\}_{k=1}^{N-1},\{\boldsymbol{P}_k,\rho_k\}_{k=1}^{N},\mathcal{L}} \quad & \sum_{k=1}^{N} J_{\mathrm{vol}}^{\mathrm{syn}}(t_k) \\
\text{s.t.} \quad & \boldsymbol{P}_k \succ 0, \quad \rho_k > 0, \qquad k = 1,\ldots,N, \\
& F_{\mathrm{syn}}(t_N) \subseteq \mathcal{X}_f, \\
& \text{funnel invariance SOS constraints hold at } t_k, \quad k = 1,\ldots,N-1, \\
& \text{actuator saturation SOS constraints hold at } t_k, \quad k = 1,\ldots,N-1, \\
& \text{bounded effect SOS constraints hold for all } \boldsymbol{w} \in W, \quad k = 1,\ldots,N-1, \\
& \bar{\boldsymbol{u}}(t_k) = -\boldsymbol{K}_k \bar{\boldsymbol{x}}(t_k), \qquad k = 1,\ldots,N-1.
\end{aligned}
\tag{46}
$$

where $\mathcal{L}$ denotes the collection of SOS multiplier polynomials. The terminal funnel is constrained by the prescribed landing requirements, while the terminal feedback gain is fixed and is therefore not included among the decision variables in (46). The representative SOS inequalities for the funnel invariance condition, actuator saturation constraints, and bounded effect constraints have been given in Section 3.2. Therefore, the synthesized controller is obtained by optimizing the feedback gain matrices together with the funnel variables so as to maximize the corresponding funnel volume metric under the prescribed terminal landing requirements, actuator saturation constraints, and disturbance bounds.

It should be noted that (46) represents the overall design objective of the synthesis procedure rather than a single SOS program solved simultaneously over the entire time horizon. Because the funnel variables, feedback gains, and SOS multipliers are bilinearly coupled, the overall objective is addressed using a backward point-by-point alternating optimization strategy over the discrete time grid. Starting from the terminal funnel, the funnel at the next time instant is treated as known. At each nonterminal time instant t_k, the current variables $\{\boldsymbol{P}_k, \rho_k, \boldsymbol{K}_k\}$ are iteratively updated. Specifically, with $\boldsymbol{P}_k$ fixed, a line search is performed over ρ_k while optimizing $\boldsymbol{K}_k$ to enlarge the funnel under the corresponding SOS constraints. Then, with $\{\boldsymbol{K}_k, \rho_k\}$ fixed, $\boldsymbol{P}_k$ is updated through heuristic shape matrix optimization to further enlarge the funnel. The SOS multipliers are subsequently updated, and the procedure is repeated until convergence before moving to the previous time instant.

If a candidate feedback gain fails to admit a feasible finite-time funnel satisfying the prescribed invariance condition, terminal landing requirements, actuator saturation constraints, and disturbance bounds, the corresponding SOS problem becomes infeasible and the candidate gain is not retained during the synthesis process. Therefore, the proposed framework does not accept or reject a controller solely according to a conventional asymptotic stability criterion. Instead, a controller is considered admissible only when a finite-time safe region satisfying all prescribed requirements can be certified.

As will be shown in Section 5.3, the resulting controller yields a larger funnel volume and improved state-wise admissible deviation bounds over a substantial portion of the landing process. It should be emphasized that the funnel is not a predefined physical safety boundary of the carrier. The terminal landing requirements, actuator saturation constraints, and disturbance bounds are prescribed independently, whereas the funnel represents the controller-dependent safe region that can be certified under these common requirements. Therefore, a larger funnel does not imply that larger tracking errors are desired or that the controller performs worse. Instead, it indicates that, under the same terminal landing requirements, actuator saturation constraints, and disturbance bounds, the controller can safely accommodate a wider range of complete six-dimensional state deviations, with the finite-time invariance property ensuring that the corresponding trajectories remain inside the time-varying funnel throughout the landing process and reach the same prescribed terminal set. Compared with conventional controller design approaches, which primarily focus on local tracking performance, funnel-based control synthesis explicitly accounts

for the evolution of the closed-loop system throughout the landing process in the multi-dimensional state space. As a result, the safety of the synthesized controller can be evaluated quantitatively through the resulting funnel rather than being assessed solely through empirical tuning or extensive Monte Carlo simulations.

The control synthesis procedure used in this paper is summarized in Table 2.

Table 2. Point-by-point funnel-based control synthesis procedure.

Algorithm for Funnel-Based Control Synthesis	
Step 0	Specify the synthesis setting and initialize the funnel variables. Choose the convergence threshold $\varepsilon > 0$, roll-back factor $b > 1$, line search interval for ρ_k, and line search tolerance. Starting from the terminal funnel, solve backward for $k = N-1, N-2, \ldots, 1$. At each time instant, initialize $\boldsymbol{P}_k = \boldsymbol{P}_{k+1}$ and $\rho_k = \rho_{k+1}$.
Step 1	Obtain a feasible initial solution for $\{\boldsymbol{P}_k, \rho_k, \boldsymbol{K}_k\}$. With $\{\boldsymbol{P}_k, \rho_k\}$ fixed and the funnel at t_{k+1} known, solve the corresponding SOS feasibility problem for $\boldsymbol{K}_k$ and the SOS multipliers. If the problem is infeasible, set $\boldsymbol{P}_k = b\boldsymbol{P}_k$ to shrink the current funnel and repeat this step. Once a feasible solution is obtained, proceed to Step 2.
Step 2	Update $\{\boldsymbol{K}_k, \rho_k\}$ with $\boldsymbol{P}_k$ fixed. With $\boldsymbol{P}_k$ and the SOS multipliers fixed, perform a line search over ρ_k. For each candidate value of ρ_k, optimize $\boldsymbol{K}_k$ subject to the corresponding SOS constraints. Retain the largest feasible value of ρ_k and the associated feedback gain matrix $\boldsymbol{K}_k$, and terminate the line search when the prescribed tolerance is reached.
Step 3	Update $\boldsymbol{P}_k$ with $\{\boldsymbol{K}_k, \rho_k\}$ fixed. With $\{\boldsymbol{K}_k, \rho_k\}$ and the SOS multipliers fixed, update $\boldsymbol{P}_k$ through the auxiliary-ellipsoid-based shape matrix optimization introduced in Section 3.2. Specifically, minimize σ_k subject to the corresponding SOS constraints and $\boldsymbol{P}_k \preceq \sigma_k \boldsymbol{S}_k$ to further enlarge the funnel.
Step 4	Check convergence. Evaluate the funnel size before Step 2 and after Step 3 according to $\mathrm{vol}_k = [\det(\boldsymbol{P}_k/\rho_k)]^{-1/2}$. If the relative improvement in vol_k is smaller than ε, terminate the iteration at the current time instant and proceed to t_{k-1}; otherwise, proceed to Step 5.
Step 5	Update the SOS multipliers. With the updated $\{\boldsymbol{P}_k, \rho_k, \boldsymbol{K}_k\}$ fixed, solve the corresponding SOS multiplier subproblem to update the auxiliary SOS multiplier polynomials, and then return to Step 2.

5. Simulations

5.1. Simulation Setup and Nominal Trajectory

The physical and aerodynamic parameters of the carrier aircraft used in the simulations are listed in Table 3, which are adopted from [32]. All numerical simulations are carried out in MATLAB R2020b. The SOS conditions involved in funnel construction and control synthesis are modeled using YALMIP and converted into semidefinite programming subproblems. The resulting subproblems are solved using MOSEK, which is selected because it directly supports the semidefinite and conic optimization structure arising from the SOS reformulation and has also been successfully used in previous funnel-based SOS implementations [27]. The backward point-by-point and alternating optimization procedures summarized in Tables 1 and 2 are implemented in MATLAB, while YALMIP and MOSEK are used to formulate and solve the convex subproblem at each iteration. The representative SOS constraints are given in Section 3.2, whereas the overall control-synthesis formulation and its alternating solution procedure are presented in Section 4.3.

Table 3. Parameters of the carrier aircraft.

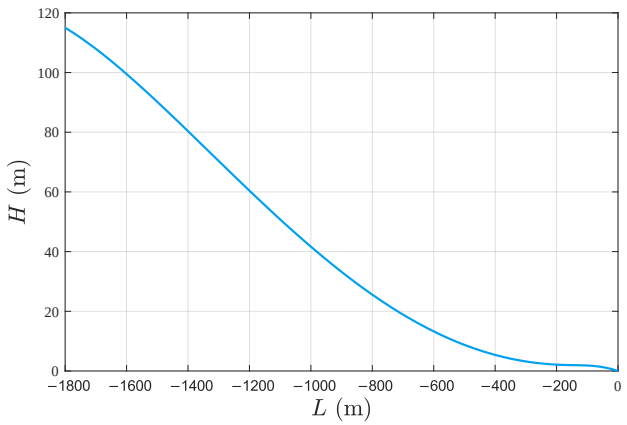
Parameter	Value
Mass m	16,374 kg
Pitch moment of inertia I	239,720 kg m^2
Reference wing area S_{ref}	37.16 m^2
Mean aerodynamic chord c	3.51 m
Drag coefficient C_{D0}	0.1423
Lift coefficient C_{L0}	0.732
Drag coefficient $C_{D\alpha}$	-0.00438
Lift coefficient $C_{L\alpha}$	0.0751
Drag coefficient $C_{D\alpha^2}$	0.0013
Lift coefficient $C_{L_{D_z}}$	0.0144
Moment coefficient C_{m0}	-0.1885
Moment coefficient $C_{m\alpha}$	-0.00437
Moment coefficient $C_{m_{D_z}}$	-0.0196
Moment coefficient $C_{m\omega}$	-0.123

Following the trajectory generation method described in Section 2, a nominal carrier landing trajectory is generated for the considered simulation scenario. The initial conditions and terminal landing requirements used in this trajectory generation are listed in Table 4.

Table 4. Initial and terminal conditions for the nominal trajectory.

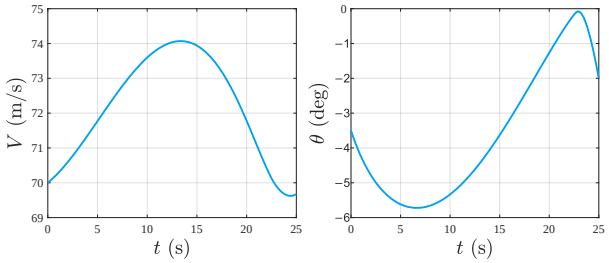
State Variable	Initial Value	Terminal Constraint
Velocity V_0	70 m s^{-1}	[68 m s^{-1}, 72 m s^{-1}]
Flight path angle θ_0	$-3.5°$	$[-2°, 2°]$
Pitch angle ϑ_0	$4.5°$	$[-2°, 2°]$
Pitch rate ω_0	$-0.5°$ s^{-1}	–
Altitude H_0	115 m	0 m
Range L_0	-1800 m	0 m

The resulting trajectory is feasible for the considered carrier landing scenario and satisfies the terminal landing requirements, as illustrated in Figure 3. Based on this nominal trajectory, a time-varying funnel is constructed to characterize the safe region of the closed-loop system. The numerical settings used for funnel construction are summarized in Table 5.

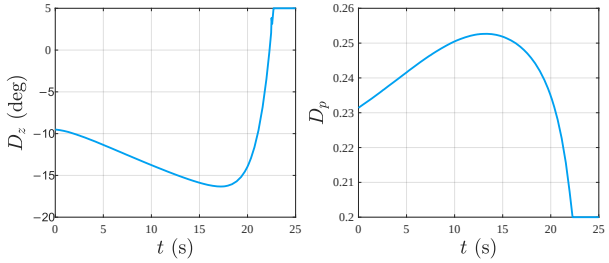


(**a**) Altitude–range trajectory.

Figure 3. *Cont.*



(**b**) Airspeed and flight path angle.



(**c**) Control inputs.

Figure 3. Nominal carrier landing trajectory.

Table 5. Numerical settings for funnel construction.

Parameter	Value (Range)
Number of discretization points N	51
Closed-loop elevator deflection constraint D_z	$[-20, 10]^\circ$
Closed-loop throttle setting constraint D_p	$[0.1, 1]$
Roll-back factor b	1.5
Convergence threshold for shape matrix ε	0.02

5.2. Validation of the Funnel-Based Safe Region in the Multi-Dimensional State Space

The simulations are conducted using the six-dimensional longitudinal model introduced in Section 2. The airspeed, altitude, and range states are scaled as

$$v = V/V_0, \qquad h = H/V_0, \qquad \ell = L/V_0, \tag{47}$$

where V_0 denotes the initial speed of the nominal landing trajectory.

A linear quadratic regulator (LQR) is employed as the baseline controller. The weighting matrices are chosen as

$$\boldsymbol{Q} = \mathrm{diag}([1\ 1\ 1\ 1\ 1\ 1]), \qquad \boldsymbol{R} = \mathrm{diag}([1\ 1]). \tag{48}$$

The resulting time-varying feedback gain matrix of the baseline controller at t_k is denoted by $\boldsymbol{K}_k^{\mathrm{LQR}}$.

The deck motion is introduced into the six-dimensional longitudinal model as an external disturbance [32], with the deck-heave velocity given by

$$\dot{h}_{\mathrm{deck}} = 1.219 \sin\left(0.6t + \frac{\pi}{2}\right) + \frac{0.707 \times 90}{57.3} \sin(0.6t). \tag{49}$$

Accordingly, the altitude dynamics is modified as

$$\dot{H} = V \sin\theta - \dot{h}_{\mathrm{deck}}. \tag{50}$$

Here, the shape matrix of the terminal set for the funnel is specified as

$$E = \mathrm{diag}\left(\left[\frac{V_0^2}{4},\ 1,\ 1,\ \frac{1}{4},\ \frac{V_0^2}{16},\ \frac{V_0^2}{4}\right]\right). \tag{51}$$

Accordingly, the terminal deviations of the closed-loop trajectory from the nominal trajectory are required to satisfy the following bounds: 2 m/s for velocity, 1°/s for flight path angle, 1°/s for pitch angle, 1°/s^2 for pitch rate, 4 m for altitude, and 2 m for range. With the deck motion applied over the time interval from 22 s to 25 s, the backward funnel is computed under the modified dynamics.

Figure 4 presents the closed-loop trajectories together with the corresponding backward funnel in the position–time space. The trajectories are generated by sampling initial states from the funnel inlet and propagating the original nonlinear longitudinal dynamics under deck motion. During this continuous-time trajectory propagation, each entry of the time-varying LQR feedback gain matrix is linearly interpolated between adjacent discrete time instants. Although the figure only shows a low-dimensional projection for visualization, the funnel membership is checked in the full six-dimensional state space. At each discrete time instant, the funnel membership of each trajectory is evaluated in the full six-dimensional state space using the corresponding level-set function. The numerical results confirm that all trajectories satisfy $V_k(\bar{x}(t_k)) \leq 1$ throughout the landing process, which validates the funnel as a safe region under the considered deck motion disturbance. Consistent with the safety interpretation of the funnel, no go-around is triggered in this case because the considered deck motion disturbance is accounted for in the funnel construction and the aircraft states remain inside the certified safe region. A go-around is triggered only when the actual aircraft state leaves the offline-computed funnel, which may occur when the actual disturbance exceeds the bound considered during funnel construction.

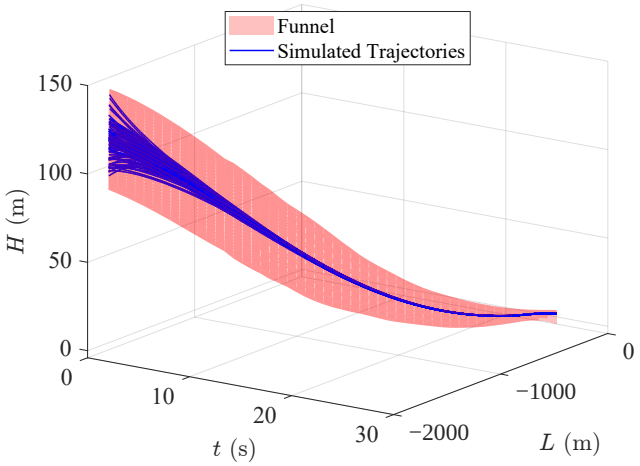


Figure 4. Verification of the funnel as a safe region in the position–time space.

Figure 5 compares the safe regions associated with the funnel-based method and the existing method [2]. The funnel-based safe region is constructed and evaluated in the full six-dimensional state space, thereby accounting for all state components throughout the landing process. Since the full six-dimensional safe region cannot be directly visualized, Figure 5 only presents its projection onto the $\overline{L}$–$\overline{H}$ subspace over time. For the existing method, the go-around decision is made based solely on altitude deviation, resulting in a relatively limited region in the displayed space. In contrast, the projection of the funnel-based safe region covers a larger region. Therefore, the comparison illustrates that the proposed method provides a less conservative and more informative safe-region characterization than the existing single-dimensional altitude deviation method.

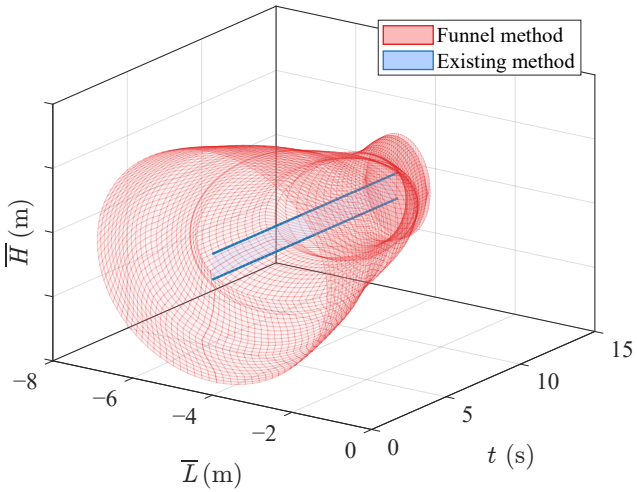


Figure 5. Comparison between the funnel-based method and the existing method in the $\overline{L}$–t–$\overline{H}$ space.

5.3. Demonstration of the Funnel-Based Safety Metric and Funnel-Based Control Synthesis

This subsection demonstrates the funnel-based safety metrics introduced in Section 4.2 and the funnel-based control synthesis method presented in Section 4.3. To this end, two closed-loop control systems are considered, namely, the baseline LQR controller and the synthesized controller obtained from the funnel-based control synthesis procedure. Both controllers use the same nominal landing trajectory and the same linear state feedback structure. For the baseline controller, the time-varying feedback gain matrix $\boldsymbol{K}_k^{\mathrm{LQR}}$ is obtained from the LQR design using the weighting matrices specified in Section 5.2. For the synthesized controller, the 12 entries of the 2×6 feedback gain matrix $\boldsymbol{K}_k^{\mathrm{syn}}$ are optimized at each nonterminal discrete time instant according to the synthesis procedure in Section 4.3, while the terminal feedback gain is kept fixed. The funnel construction, control synthesis, and funnel-based metric evaluation are performed at the discrete time instants t_k, and therefore no intermediate feedback gain values are used in the metric comparisons presented in this subsection. For the continuous-time closed-loop trajectory propagation used to validate the funnel in Section 5.2, each entry of the baseline time-varying feedback gain matrix is linearly interpolated between adjacent discrete time instants. Therefore, the differences between the resulting funnels reflect the effects of the optimized feedback gains rather than changes in the prescribed landing conditions.

To further clarify how the controller parameters are modified by the synthesis procedure, Table 6 compares all 12 entries of the feedback gain matrices of the baseline and synthesized controllers at a representative nonterminal time instant, $t_k = 10$ s. The results show that the synthesis procedure directly modifies the feedback gains associated with both control channels while retaining the same linear state feedback structure.

Table 6. Comparison of the feedback gains of the baseline LQR and synthesized controllers at $t_k = 10$ s.

State	k_{1j}^{LQR}	k_{1j}^{syn}	k_{2j}^{LQR}	k_{2j}^{syn}
V	0.829	1.109	5.158	5.013
θ	−1.939	−1.659	1.137	0.857
ϑ	−4.599	−4.391	0.420	0.384
ω	−0.414	−0.370	0.032	0.057
H	−0.874	−0.743	0.485	0.348
L	0.472	0.606	0.854	0.574

Based on the funnel volume metric introduced in Section 4.2, the resulting safe regions of the two controllers are then compared from the perspective of overall funnel volume.

For the present control synthesis results, the synthesized funnel is characterized jointly by $\boldsymbol{P}_k$ and ρ_k. Therefore, the scalar quantity $-\log\det(\boldsymbol{P}_k/\rho_k)$ is adopted here as the funnel volume metric for comparing the overall size of the two funnels at each time instant.

Figure 6 compares the funnel volume metric associated with the baseline and synthesized controllers over the entire landing process. The percentage improvements reported below are calculated from the corresponding six-dimensional ellipsoidal volume ratios, rather than from percentage changes in the log-determinant metric. Quantitatively, the synthesized controller improves the average funnel volume over the main landing interval from 0 to 20 s by 1887.75%, while the median and peak volume improvements over the full time horizon reach 1737.85% and 3998.82%, respectively. These results indicate that, under identical task requirements and constraints, the synthesized controller yields a substantially larger funnel volume over most of the landing process. As the terminal time is approached, the difference between the two curves gradually decreases, since both funnels are required to satisfy the same terminal precision requirements.

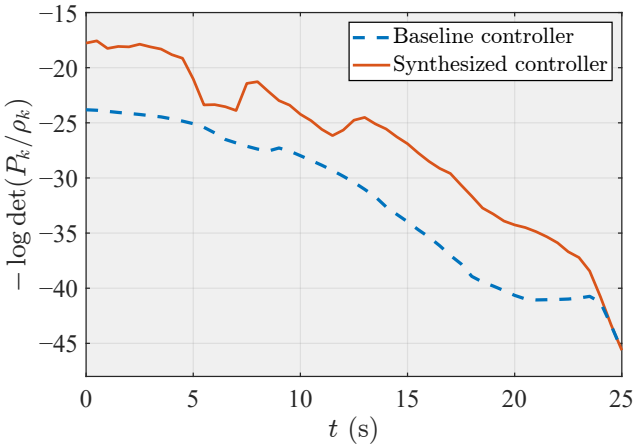


Figure 6. Comparison of the funnel volume metric $-\log\det(P_k/\rho_k)$ between the baseline controller and the synthesized controller.

In addition to the overall funnel volume comparison, the state-wise admissible deviations provide a more detailed metric for examining how the safe region changes along representative state dimensions. Specifically, for each state dimension, the admissible deviation bound is quantified by the square root of the corresponding diagonal entry of the inverse matrix defining the funnel. For the synthesized controller, this state-wise metric is evaluated from $(P_k/\rho_k)^{-1}$, whereas for the baseline controller it reduces to P_k^{-1} since $\rho_k = 1$. In the present paper, three representative state dimensions are selected, namely, velocity, altitude, and range, since they are directly related to the longitudinal landing performance and are also the most physically interpretable in the present carrier-landing scenario.

Figure 7 shows the comparison of the state-wise admissible deviations associated with the baseline and synthesized controllers. Quantitatively, over the main landing interval from 0 to 20 s, the synthesized controller increases the average admissible deviation bound by 72.22% in velocity, 405.54% in altitude, and 82.03% in range. Over the full time horizon, the corresponding peak improvements reach 136.36%, 611.40%, and 208.05%, respectively. These results indicate that the synthesized controller not only enlarges the overall funnel volume, as shown in Figure 6, but also improves the state-wise admissible deviations along representative dimensions of the closed-loop system. Meanwhile, the extent of improvement is not uniform across different state dimensions or different time instants, which further reflects the time-varying and multi-dimensional nature of the funnel-

based safe region. As the terminal time is approached, the differences between the two funnels gradually decrease, since both controllers are required to satisfy the same terminal precision requirements.

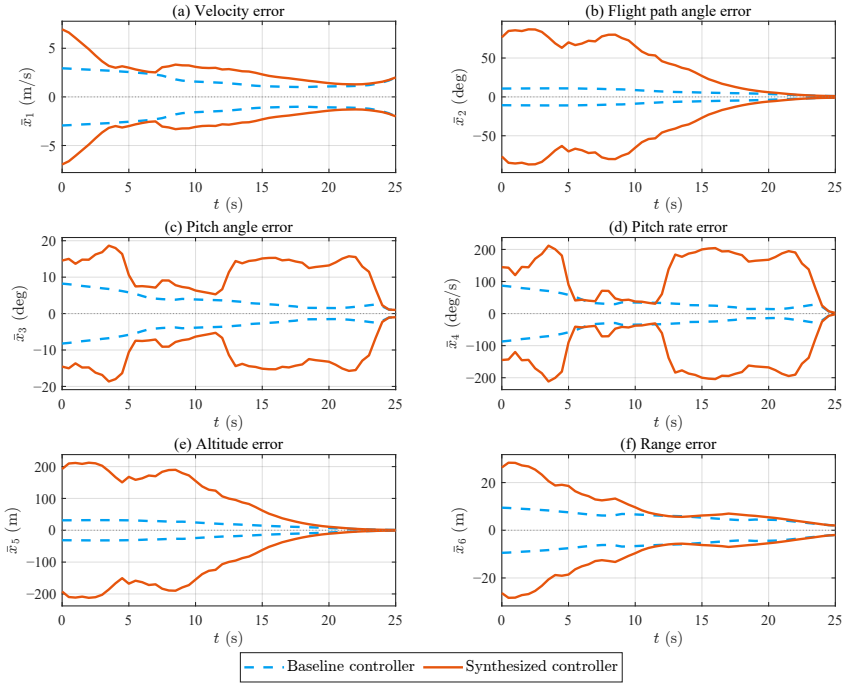


Figure 7. Comparison of the state-wise admissible deviations between the baseline controller and the synthesized controller.

To provide a compact quantitative summary, the main results of the global funnel volume comparison and the representative state-wise comparisons are listed in Table 7.

Table 7. Quantitative summary of the funnel-based safety metric comparison between the baseline and synthesized controllers.

Metric Category	Quantity	Improvement
Global funnel volume metric	Average volume improvement over 0–20 s	1887.75%
Global funnel volume metric	Median volume improvement over full time horizon	1737.85%
Global funnel volume metric	Peak volume improvement over full time horizon	3998.82%
Representative state-wise metric	Velocity: average improvement over 0–20 s	72.22%
Representative state-wise metric	Velocity: peak improvement over full time horizon	136.36%
Representative state-wise metric	Altitude: average improvement over 0–20 s	405.54%
Representative state-wise metric	Altitude: peak improvement over full time horizon	611.40%
Representative state-wise metric	Range: average improvement over 0–20 s	82.03%
Representative state-wise metric	Range: peak improvement over full time horizon	208.05%

Taken together, the results in Figures 6 and 7, together with the quantitative summary in Table 7, demonstrate the effect of the funnel-based control synthesis method from both global and state-wise perspectives. Under the same task requirements and constraints, the synthesized controller is associated with a larger funnel volume and improved state-wise admissible deviations over a substantial portion of the landing process. These results further show that the proposed framework can serve not only as a quantitative safety evaluation tool for different closed-loop control systems, but also as an effective criterion for controller parameter optimization.

6. Conclusions

This paper proposes a funnel-based safety-guaranteed go-around decision framework for ACLSs, and further develops quantitative funnel-based safety metrics together with a safety-metric-driven control synthesis method. The main conclusions are as follows:

(1) A funnel-based go-around decision framework is established for ACLSs. By constructing a backward funnel around the nominal landing trajectory, the safe region of the closed-loop system is explicitly characterized in a time-varying multi-dimensional state space under the considered nonlinear dynamics, actuator saturation constraints, terminal landing-precision requirements, and disturbance bounds. Based on the invariance property of the funnel, the online go-around decision can be made directly by checking whether the real-time aircraft state remains inside the funnel. Compared with the traditional method based on a single-dimensional altitude deviation criterion, the proposed framework provides a less conservative and more informative basis for safe and precise go-around decisions.

(2) Quantitative funnel-based safety metrics are established for ACLSs. By using the funnel as the safe region associated with a given closed-loop control system, the safety of ACLSs can be evaluated quantitatively through the global funnel volume metric and the state-wise admissible deviation metrics. These two types of metrics characterize the safety of ACLSs from global and state-wise perspectives, respectively. Simulation results further show that the proposed funnel-based method provides a larger safe region than the existing altitude-deviation-based method under the considered deck motion disturbance, while maintaining the required safety guarantee.

(3) A safety-metric-driven control synthesis method is developed. By using the funnel volume metric as the optimization criterion, the controller parameters and the associated funnel are jointly optimized so as to enlarge the safe region under the same task requirements and constraints. Quantitative simulation results show that the synthesized controller yields a substantially larger funnel volume than the baseline controller. In particular, the average funnel volume improvement over the main landing interval reaches 1887.75%, while representative state-wise admissible deviations are also improved, including 72.22% in velocity, 405.54% in altitude, and 82.03% in range over 0–20 s. These results indicate enhanced tolerance to state deviations and a larger safe region for the closed-loop system. Therefore, the proposed framework can serve not only as a tool for safety evaluation, but also as an effective criterion for safety-oriented controller optimization.

This work focuses on funnel construction, safety evaluation, and control synthesis for a given nominal landing trajectory under prescribed disturbance bounds. The current validation is primarily numerical and simulation-based, and the considered disturbance model remains relatively limited compared with actual carrier-operating conditions. Therefore, the practical conclusions should be understood within the scope of the adopted nonlinear longitudinal model and prescribed disturbance bounds. Future research will further incorporate more realistic combined disturbances, including atmospheric disturbances together with deck motion.

Author Contributions: Methodology, Y.L.; writing—original draft preparation, Z.L.; writing—review and editing, W.M.; supervision, J.L. All authors have read and agreed to the published version of the manuscript.

Funding: This research was funded by the Fundamental and Interdisciplinary Disciplines Breakthrough Plan of the Ministry of Education of China, Grant No. JYB2025XDXM116.

Data Availability Statement: Data is contained within the article.

Conflicts of Interest: The authors declare no conflicts of interest. The funder had no role in the design of the study; in the collection, analyses, or interpretation of data; in the writing of the manuscript; or in the decision to publish the results.

References

1. Zhen, Z.; Wang, X.; Jiang, J.; Yang, Y. Research progress in guidance and control of automatic carrier landing of carrier-based aircraft. *Acta Aeronaut. Astronaut. Sin.* **2017**, *38*, 020435. [CrossRef]
2. Zhang, Z.; Zhen, Z. Research progress on guidance and control of fixed-wing manned and unmanned carrier-based aircraft landing. *Acta Aeronaut. Astronaut. Sin.* **2025**, *46*, 532336. [CrossRef]
3. Pravitra, J.; Clarke, J.-P.B.; Johnson, E.N. Landing a fixed-wing UAV on a moving platform: A pseudospectral optimal control approach. In Proceedings of the AIAA Aviation 2019 Forum, Dallas, TX, USA, 17–21 June 2019; Paper AIAA 2019-3257. [CrossRef]
4. Urnes, J.M.; Hess, R.K. Development of the F/A-18A automatic carrier landing system. *J. Guid. Control Dyn.* **1985**, *8*, 289–295. [CrossRef] [PubMed]
5. Reiner, J.; Balas, G.J.; Garrard, W.L. Robust dynamic inversion for control of highly maneuverable aircraft. *J. Guid. Control Dyn.* **1995**, *18*, 18–24. [CrossRef] [PubMed]
6. Singh, S.; Padhi, R. Automatic path planning and control design for autonomous landing of UAVs using dynamic inversion. In Proceedings of the 2009 American Control Conference, St. Louis, MO, USA, 10–12 June 2009; pp. 2409–2414. [CrossRef]
7. Ma, Y.; Guan, Z.; Zheng, Z. Nonlinear control for automatic carrier landing with deck motion compensation. In Proceedings of the 37th Chinese Control Conference (CCC), Wuhan, China, 25–27 July 2018; pp. 9883–9888. [CrossRef]
8. Reed, S.; Steck, J.E. Adaptive control for fault tolerant autonomous carrier recovery. In Proceedings of the AIAA Guidance, Navigation, and Control Conference, Kissimmee, FL, USA, 8–12 January 2018; Paper AIAA 2018-0871. [CrossRef]
9. Zhen, Z.; Tao, G.; Yu, C.; Xue, Y. A multivariable adaptive control scheme for automatic carrier landing of UAV. *Aerosp. Sci. Technol.* **2019**, *92*, 714–721. [CrossRef]
10. Zhu, Q.; Yang, Z. Dynamic recurrent fuzzy neural network-based adaptive sliding control for longitudinal automatic carrier landing system. *J. Intell. Fuzzy Syst.* **2019**, *37*, 53–62. [CrossRef]
11. Yu, Y.; Wang, H.; Li, N.; Su, Z.; Wu, J. Automatic carrier landing system based on active disturbance rejection control with a novel parameters optimizer. *Aerosp. Sci. Technol.* **2017**, *69*, 149–160. [CrossRef]
12. Chen, M.; Zou, Q.; Jiang, C.; Wu, Q. Dynamical inversion flight control based on neural network disturbance observer. *Control Decis.* **2008**, *23*, 283–287.
13. Hu, W.; Wan, W.; Chen, M. Neural network and disturbance observer based control for automatic carrier landing of UAV. *Acta Aeronaut. Astronaut. Sin.* **2022**, *43*, 726963. [CrossRef]
14. Guan, Z.; Liu, H.; Zheng, Z.; Lungu, M.; Ma, Y. Fixed-time control for automatic carrier landing with disturbance. *Aerosp. Sci. Technol.* **2021**, *108*, 106403. [CrossRef]
15. Duan, H.; Yuan, Y.; Zeng, Z. Automatic carrier landing system with fixed time control. *IEEE Trans. Aerosp. Electron. Syst.* **2022**, *58*, 3586–3600. [CrossRef]
16. Yuan, Y.; Duan, H.; Zeng, Z. Automatic carrier landing control with external disturbance and input constraint. *IEEE Trans. Aerosp. Electron. Syst.* **2023**, *59*, 1426–1438. [CrossRef]
17. Zhou, H.T.; Zheng, Z.W.; Guan, Z.Y.; Ma, Y.P. Control barrier function based nonlinear controller for automatic carrier landing. In Proceedings of the 16th International Conference on Control, Automation, Robotics and Vision (ICARCV), Shenzhen, China, 13–15 December 2020; pp. 584–589. [CrossRef]
18. Lu, K.; Liu, C. A L1 adaptive control scheme for UAV carrier landing using nonlinear dynamic inversion. *Int. J. Aerosp. Eng.* **2019**, *2019*, 6917393. [CrossRef]
19. Zheng, Z.; Jin, Z.; Sun, L.; Zhu, M. Adaptive sliding mode relative motion control for autonomous carrier landing of fixed-wing unmanned aerial vehicles. *IEEE Access* **2017**, *5*, 5556–5565. [CrossRef]
20. Zhang, Y.; Wang, S.; Chang, B.; Wu, W. Adaptive constrained backstepping controller with prescribed performance methodology for carrier-based UAV. *Aerosp. Sci. Technol.* **2019**, *92*, 55–65. [CrossRef]
21. Guan, Z.; Ma, Y.; Zheng, Z.; Guo, N. Prescribed performance control for automatic carrier landing with disturbance. *Nonlinear Dyn.* **2018**, *94*, 1335–1349. [CrossRef]
22. Zhen, Z.; Jiang, S.; Ma, K. Automatic carrier landing control for unmanned aerial vehicles based on preview control and particle filtering. *Aerosp. Sci. Technol.* **2018**, *81*, 99–107. [CrossRef]
23. Zhen, Z.; Jiang, S.; Jiang, J. Preview control and particle filtering for automatic carrier landing. *IEEE Trans. Aerosp. Electron. Syst.* **2018**, *54*, 2662–2674. [CrossRef]
24. Zhen, Z.; Peng, M.; Xue, Y.; Jiang, S. Robust preview control and autoregressive prediction for aircraft automatic carrier landing. *IEEE Access* **2019**, *7*, 181273–181283. [CrossRef]

25. Misra, G.; Bai, X. Output-feedback stochastic model predictive control for glideslope tracking during aircraft carrier landing. *J. Guid. Control Dyn.* **2019**, *42*, 2098–2105. [CrossRef]
26. Cui, K.; Han, W.; Sun, C.; Su, X.; Liu, J. Receding horizon longitudinal control technology for automatic carrier landing with variable reference trajectory based on sliding rate information. *IEEE Access* **2020**, *8*, 214742–214755. [CrossRef]
27. Liu, Y.; Wang, M.; Luo, J.; Li, J.; Cheng, X.; Ding, J.; Sun, K. A tracking guidance method with funnel scheduling for Mars landing. *Aerosp. Sci. Technol.* **2024**, *155*, 109738. [CrossRef]
28. Tang, Y.; Zhu, Z.; Zhang, H.; Luo, J.; Yuan, J. A tutorial and review on robot motion planning. *Acta Aeronaut. Astronaut. Sin.* **2023**, *44*, 26495. [CrossRef]
29. Tedrake, R.; Manchester, I.R.; Tobenkin, M.; Roberts, J.W. LQR-trees: Feedback motion planning via sums-of-squares verification. *Int. J. Robot. Res.* **2010**, *29*, 1038–1052. [CrossRef]
30. Gao, D. Research on the Computation of Reachable Sets and the Feedback Motion Planning for Nonlinear Systems. Ph.D. Thesis, Northwestern Polytechnical University, Xi'an, China, 2020.
31. Liu, Y.; Wang, M.; Luo, J. Powered descent funnel control synthesis based on the sum-of-squares programming. *IEEE Trans. Aerosp. Electron. Syst.* **2025**, *61*, 13407–13418. [CrossRef]
32. Bian, Q. Research on Flight Control Technology for Carrier-Based Aircraft Landing. Ph.D. Thesis, Northwestern Polytechnical University, Xi'an, China, 2019.

Disclaimer/Publisher's Note: The statements, opinions and data contained in all publications are solely those of the individual author(s) and contributor(s) and not of MDPI and/or the editor(s). MDPI and/or the editor(s) disclaim responsibility for any injury to people or property resulting from any ideas, methods, instructions or products referred to in the content.